Full length article

# Deformation dynamics of a neutron-irradiated aluminum alloy: An *in situ* synchrotron tomography study

H.W. Chai [a], D. Fan [c], J.C. Yuan [a], L. Hu [d,*], H.L. Xie [f], G.H. Du [f], Q.J. Feng [e], W. Zhou [e], J.Y. Huang [b,c,*]

[a] *School of Materials Science and Engineering, Southwest Jiaotong University, Chengdu, Sichuan, PR China*
[b] *MOE Key Laboratory of Impact and Safety Engineering, Ningbo University, Ningbo, Zhejiang, PR China*
[c] *The Peac Institute of Multiscale Sciences, Chengdu, Sichuan, PR China*
[d] *Laboratory for Shock Wave and Detonation Physics, Institute of Fluid Physics, China Academy of Engineering Physics, Mianyang, Sichuan, China*
[e] *Institute of Nuclear Physics and Chemistry, China Academy of Engineering Physics, Mianyang, Sichuan, China*
[f] *Shanghai Institute of Applied Physics, Chinese Academy of Sciences, Shanghai, PR China*

## ARTICLE INFO

## ABSTRACT

To reveal the effects of long-term neutron irradiation on the mechanical behavior of nuclear materials, *in situ* quasi-static uniaxial tensile tests are conducted on an LT21 aluminum (Al) alloy from a decommissioned research reactor. Scanning/Transmission electron microscopy (SEM/TEM), and micro CT are first applied to characterize the microstructures of LT21 Al alloys aged naturally and neutron-irradiated for 30 years. *In situ* synchrotron micro computed tomography (CT) is adopted to characterize the deformation and damage dynamics of this LT21 Al. A new particle tracking analysis technique is proposed to quantify the displacement/strain fields and microstructural evolution (e.g., particle movement and pore growth) in the irradiated sample. Long-term irradiation induces considerable microstructural changes in the LT21 Al alloy, including the precipitation/aggregation of micron-sized Si particles and nanoscale $Mg_2Si$ particles. In addition, the size of pores and particles in the irradiated material appear considerably larger than that in the unirradiated material. During tension, the alloy undergoes elastic-plastic deformation followed by shear-dominated necking failure. The porosity and pore size exhibits an overall increase with increasing loading. Formation of new pores occurs in two modes, formation at the particle-matrix interfaces and random formation across the sample. For mode one, pores tend to nucleate at the top and bottom ends of a particle (relative to the loading direction). Formation of new pores and growth of initial and newly-nucleated pores occur simultaneously and contributes approximately equally to damage accumulation in the irradiated LT21 Al alloy before necking occurs. The deformation dynamics deepens our understanding of the aging of nuclear materials.

## 1. Introduction

Radiation resistance of materials is significant for various applications such as nuclear power [1–4], outer space structures [5] and industrial applications [6,7]. Materials under irradiation by high-energy particles, such as neutrons, ions and electrons, develop point defects or defect clusters, which may subsequently grow into microstructural flaws [1,8–10]. Such flaws deteriorate mechanical properties of irradiated materials [11,12], and may induce abrupt structural failure. Neutron irradiation damage of materials limit the lifetime of pressure vessels of nuclear reactors [13,14], and

constrain the choice of materials for fusion-based alternative energy sources. Neutron irradiation effects on microstructures and mechanical properties of nuclear materials are crucial for safety assessment and design optimization of nuclear reactors [15], but have been rarely investigated, especially under low-dose-rate, long-term, neutron radiation environments.

Aluminum alloys have been widely used as structural materials in research or production reactors for their small neutron absorption cross section, fast attenuation of radiation energy, and good low-temperature radiation resistance [14,16,17]. Extensive studies have been devoted to studying the evolution of mechanical properties and microstructural features (voids/pores, precipitates) of various Al alloys (e.g., 6061 Al [18–20], Fe-Cr-Al [12,21,22], and Cu-Al [23]), after ion or short-term neutron irradi-

**Nomenclature**

| | |
|---|---|
| $x, y, z$ | Coordinate axes |
| $\alpha, \beta, \omega$ | Subscripts, corresponding to the $x$, $y$, $z$-axes, respectively |
| $i$ | Deformation stage number |
| $R_\alpha$ | Eigenvalues of the gyration tensor |
| $S_G$ | Sphericity |
| EI | Elongation index |
| FI | Flatness index |
| $C$ | Correlation criterion for particle tracking |
| $C_d$ | Correlation criterion for pore tracking |
| $K$ | Moving direction identifier |
| $x_\alpha^{(m)}$ | Barycenter coordinates of particle $m$ |
| $\Delta x_\alpha$ | Difference in barycenter coordinates of particles $m$ and $n$ |
| $\sigma_\alpha$ | Weight factors of displacements in three directions |
| $\sigma_g$ | Global weight factor of displacement |
| $V_a^{(m)}$ | Volume of particle $m$ |
| $\Delta V_a$ | Volume difference between particles $m$ and $n$ |
| $\overline{V}_a$ | Average volume of particles $m$ and $n$ |
| $\lambda_\alpha$ | $R_\alpha$ ratio of particles $m$ and $n$ |
| $\mathbf{u}$ | Displacement vector |
| $u_z$ | $z$-component of $\mathbf{u}$ |
| $E_{zz}$ | Normal Lagrangian-Green strain along the $z$-axis |
| $\delta$ | Half statistical interval length |
| $L_b$ | Distance between the barycenter of a pore to that of its nearest neighbor particle |
| $f_i(L_b)$ | Probability density of $L_b$ at the $i$th deformation stage |
| $M_i(L_b)$ | Number of $L_b$ at the $i$th deformation stage |
| $N_{b,i}$ | Total number of pores at the $i$th deformation stage |
| $g_{II}$ | Probability density of pore formation via mode II |
| $G_{II}$ | Cumulative probability of pore formation via model II |
| $P_{II}$ | Total probability of random pore formation across the sample |
| $V_s$ | Sample volume |
| $\rho_a$ | Volume density of particles |
| $\theta_a$ | Angle between particle-pore connections and the $z$-axis |
| $h_i(\theta_a)$ | Probability density of $\theta_a$ at the $i$th deformation stage |
| $S_i(\theta_a)$ | Number of $\theta_a$ at the $i$th deformation stage |
| $N_{a,i}$ | Total number of particles at the $i$th deformation stage |
| $Q_{b,i}$ | Number of pores tracked at the $i$th deformation stage |
| $V_{b,i}$ | Total volume of pores at the $i$th deformation stage |
| $V_{b,i}^{(k)}$ | Volume of pore $k$ at the $i$th deformation stage |
| $\psi_i(z)$ | Average volume growth rate of pores at a specific sample height $z$ at the $i$th deformation stage |
| $\eta_i$ | Normalized porosity increase at the $i$th deformation stage |
| $\xi_i$ | Contribution of pore growth to the porosity increase at the $i$th deformation stage |
| $z_{p,i}$ | Height of upper boundaries of the necking region at the $i$th deformation stage |
| $z_{n,i}$ | Height of lower boundaries of the necking region at the $i$th deformation stage |
| $V_{b,i}(z)$ | Total volume of pores in a 50 μm thick neighborhood centered at height $z$ at the $i$th deformation stage |

ation. High-resolution transmission electron microscopy (TEM) revealed irradiation-induced dislocation loops, pores and precipitates (e.g., $Mg_2Si$, Si) in irradiated 6061Al, and the exact microstructural features (type and size) depend on irradiation temperature and dose [21]. Such defects act as dislocation barriers and promote yield/tensile strength [11,13,22]. However, they may also act as nucleation sites of damage and hence reduce ductility [11,12]. How pores and precipitates affect damage nucleation in irradiated materials under mechanical loading is an intriguing but pending question [24].

Nuclear materials in reactors are generally subjected to low-dose-rate, long-term (tens of years), neutron irradiation [25–27]. Their microstructures (including defects) and mechanical properties may be different from those subjected to high-dose-rate, short-term, neutron irradiation. Results from ion or short-term neutron irradiation may not represent the real service conditions in reactors [27,28]. Investigations on nuclear materials from decommissioned reactors can help understand radiation damage [27] and thus reactor aging, but are scarce owing to the difficulty in accessing such materials. For instance, small-angle neutron scattering revealed a pronounced change in defect size and density in a CAB-1 Al alloy after neutron irradiation for 13 years [26]. The volume fraction of defects increases by 10% due to irradiation. TEM characterizations of a low-nickel austenitic stainless steel after 30 years' nuclear service show that irradiation at low dose rates for many years results in different precipitate morphologies and hence different associated changes in matrix composition from those generated at higher dose rates [25]. It is natural to ask how the low-dose-rate, long-term, neutron irradiation changes microstructures of Al alloys, and what the link is between microstructural changes and mechanical degradation of irradiated Al alloys.

In previous studies, microstructural characterizations of irradiated materials were largely conducted via TEM [21,29], electron tomography [30] and atom-probe tomography [21,27,31]. These techniques have high spatial resolution for nanoscale features, but a limited field of view ($< 100$ μm) which are not adequate for reliable statistical analysis. Recently, synchrotron-based micro computed tomography (CT) has been adopted to map defect structures of irradiated materials (e.g., uranium alloys [28], nuclear graphite [4,32], and polyurethane foam [33]), and has been proved useful for visualizing radiation damage nondestructively in three dimensions. Synchrotron-based micro CT offers high spatial resolution without sacrificing statistical reliability. Nevertheless, *in situ* CT [4,34] characterization of the deformation dynamics of irradiated materials under mechanical loading has not been reported yet. In addition, Al shows much lower absorption of X-rays than high-$Z$ materials like U. The overall contrast between tiny defects and Al matrix may appear lower than that for U alloys [28]. Thus, image segmentation is more challenging for quantitative analysis of irradiated microstructures of Al alloys.

Al-Mg-Si alloys, with excellent mechanical and forging properties, have been widely used in reactor structures with certain strength requirements [18,19], like fuel cladding, core shroud and loop cover plate in low-temperature reactors. In this work, quasi-static tensile tests are carried out on a representative Al-Mg-Si alloy, labelled LT21, from a decommissioned research reactor. *In situ* synchrotron CT is for the first time, applied to characterize the deformation and damage dynamics of this LT21 Al alloy. Micron-sized pores and second-phase particles (precipitates) distribute uniformly across the irradiated sample prior to loading. During tension, new pores nucleate adjacent to the particles, while the initial and nucleated pores show minor growth until necking occurs in the sample. The deformation dynamics deepens our understanding of the aging of nuclear materials.

## 2. Material and methods

### 2.1. In situ CT under unixial tension

A home-made material testing system (MTS) device is used for *in situ* X-ray micro CT under uniaxial tension at the X-ray Imaging and Biomedical Application Beamline (BL13W1) of the Shanghai Synchrotron Radiation Facility [35,36]. The voxel size is 0.87 μm, and the corresponding spatial resolution is about 3 μm, which can provide deformation details of irradiation-induced defects. A dog-bone shaped sample is fabricated from the initial alloy block. The gauge length is 4.0 mm, while the dimensions of the gauge cross-section are $1.0 \times 1.0$ mm$^2$. The sample is clamped between two steel grips in a polycarbonate (PC) tube [37]. The upper grip is lifted to apply tension loading while the lower grip is fixed. Tension loading and CT scan are carried out alternately in a step-hold mode [34].

One or two scans are performed along the sample height direction to cover the region of interest at each deformation stage. X-rays transmitted through the sample impinge on the scintillator and the projections are captured with a camera for three-dimensional (3D) reconstruction. The X-ray energy is set at 24.9 keV, and the sample-to-scintillator distance is 60 mm. The exposure time is 1 s. The force–displacement curve recorded with MTS is used to calculate the engineering stress–strain curve. The loading velocity is set at 4.0 μm s$^{-1}$, corresponding to a nominal strain rate of 0.001 s$^{-1}$.

Each tomography scan comprises 1500 projections in 0°–180°, which are then reconstructed into a 3D image with software *PITRE* [38]. To quantify 3D microstructures (pores and particles), the 3D grayscale images are processed as follows. Firstly, the edges of a 3D image are removed to avoid boundary noise from phase contrast. Secondly, a non-local means filter method [39] is adopted for noise reduction. Pores and particles are then extracted by the top-hat method [40], followed by an image repair step to remove artifacts. In addition, the pores or particles whose volumes are below 14.8 μm$^3$ (equivalent diameter ∼3 μm) are removed to reduce the noise. After pores and particles are extracted accurately from the 3D images, the gyration tensor analysis (GTA) is applied to quantify their morphological information including size, shape and orientation [34,41,42]. A gyration tensor is derived from the voxel set of a pore or particle. Then the shape indices, including sphericity ($S_G$), elongation index (EI) and flatness index (FI), can be defined with the three eigenvalues of the gyration tensor [42] as

$$S_G = 1 - \frac{1}{2} \frac{\sum_{\alpha > \beta} \left( R_\alpha - R_\beta \right)^2}{\left( \sum_\alpha R_\alpha \right)^2}, \tag{1}$$

$$EI = R_2/R_1; \quad FI = R_3/R_2. \tag{2}$$

Here $R_\alpha$ ($\alpha = 1,2,3$) are the eigenvalues of the gyration tensor, and $R_1 > R_2 > R_3$.

To map the local deformation of the Al matrix, the particles and pores are tracked via 3D correlation between the reference and current tomograms, namely, the particle tracking analysis (PTA). A detailed description of the flowchart and correlation criterion of the PTA algorithm is presented in Appendix A.

### 2.2. Material and characterization

The experimental material is an LT21 Al alloy sampled from the reactor core board of a decommissioned research reactor after 30 years' service. The accumulated neutron dose is ∼ $2.15 \times 10^{21}$ n cm$^{-2}$, including about $4.30 \times 10^{20}$ n cm$^{-2}$ fast neutrons (above 0.1 MeV), $1.18 \times 10^{21}$ n cm$^{-2}$ thermal neutrons (below 0.625 eV), and about $5.40 \times 10^{20}$ n cm$^{-2}$ intermediate neutrons (between

**Table 1**
Chemical composition of LT21 (wt%) before and after irradiation.

| Elements | Al | Mg | Si | Fe |
|---|---|---|---|---|
| Unirradiated | Balance | 0.551 | 0.759 | 0.128 |
| Irradiated | Balance | 0.674 | 0.773 | 0.150 |

0.625 eV and 0.1 MeV). During service, the material is immersed in cooling water with an ambient temperature of 20–40°C, depending on the reactor core operation power. The composition, microstructure, and phases of the LT21 Al alloy before and after neutron-irradiation (prior to tensile loading) are characterized by electron backscattering diffraction (EBSD), energy dispersive X-ray spectroscopy (EDS), electron probe microanalysis (EPMA) and X-ray diffraction (XRD). EBSD and EDS are conducted with an FEI Quanta 250 FEG scanning electron microscope (SEM). EPMA is conducted with a JEOL electron probe microanalyzer, and XRD, with a PANalytical Empyrean diffractometer with an X-ray wavelength 0.154 nm. The chemical compositions of the LT21 Al before and after irradiation are measured with the inductively coupled plasma atomic emission spectroscopy. The compositions are similar before and after the neutron irradiation (Table 1).

EBSD and EDS results for the LT21 Al alloy before and after irradiation prior to loading are presented in Fig. 1a and b, respectively. The element distribution maps for Si, Mg, and Fe are overlaid on an inverse pole figure (IPF) map of the Al matrix. For clarity, the element distribution maps are shifted horizontally by a small amount relatively to each other. Three types of second-phase particles are observed across the Al matrix, i.e., pure Si, MgSi compound and AlFeSi compound in both the unirradiated and irradiated materials. The Si particles are mostly sub-circular and statistically smaller in size but larger in number than the other two types of particles. Nevertheless, the unirradiated (Fig. 1a) and (irradiated (Fig. 1b) alloy show different microstructures (grain size, and particle type and number). Grain size of the irradiated material is larger than that of the unirradiated material (60 μm versus 50 μm). No significant increase in the areal density of Si particles is observed in the irradiated material. In addition, the AlFeSi particles in the irradiated material are largely needle-shaped, but are largely plate-shaped in the unirradiated material. The XRD pattern of the material shows four phases, i.e. Al, Si, AlFeSi and Mg$_2$Si. According to previous studies [43], AlFeSi particles in Al-Mg-Si alloys can be divided into two types, $\alpha$-AlFeSi (Al$_{8.3}$Fe$_2$Si) and $\beta$-AlFeSi (Al$_{8.9}$Fe$_2$Si$_2$), which are plate-shaped (sub-circular in two dimensions) and needle-shaped, respectively. Both types of AlFeSi particles exist in the irradiated LT21 Al alloy.

Characterizations down to the nanoscale with transmission electron microscopy (TEM) are conducted on the irradiated LT21 Al alloy (Fig. 2). A large number of needle-shaped particles (marked by the arrows) 50–100 nm thick are observed (Fig. 2a), but such particles are absent in the unirradiated alloy. The TEM micrograph in Fig. 2b and the corresponding EDS map (Fig. 2d) indicates the existence of nanoscale needle-shaped Mg$_2$Si particles. The TEM images in Fig. 2c, g and h and the corresponding EDS maps (Fig. 2e, i and j) reveal other types of particles in the irradiated alloy, including needle-shaped (Fig. 2c) and plate-shaped (Fig. 2g and h) AlFeSi particles, and micron-sized elliptical Mg$_2$Si particles. The typical thickness of $\beta$-AlFeSi is 0.5–8 μm. It is interesting to note that four elements (Al, Mg, Si and Fe) are detected simultaneously in some elliptical particles which are probably the aggregates of Mg$_2$Si and AlFeSi particles (Fig. 2i and j). Apart from the second-phase particles, there exist a large number of dislocations in the irradiated material (Fig. 2f), which are not observed in the unirradiated material. Neither nanoscale pores nor helium bubbles are observed in
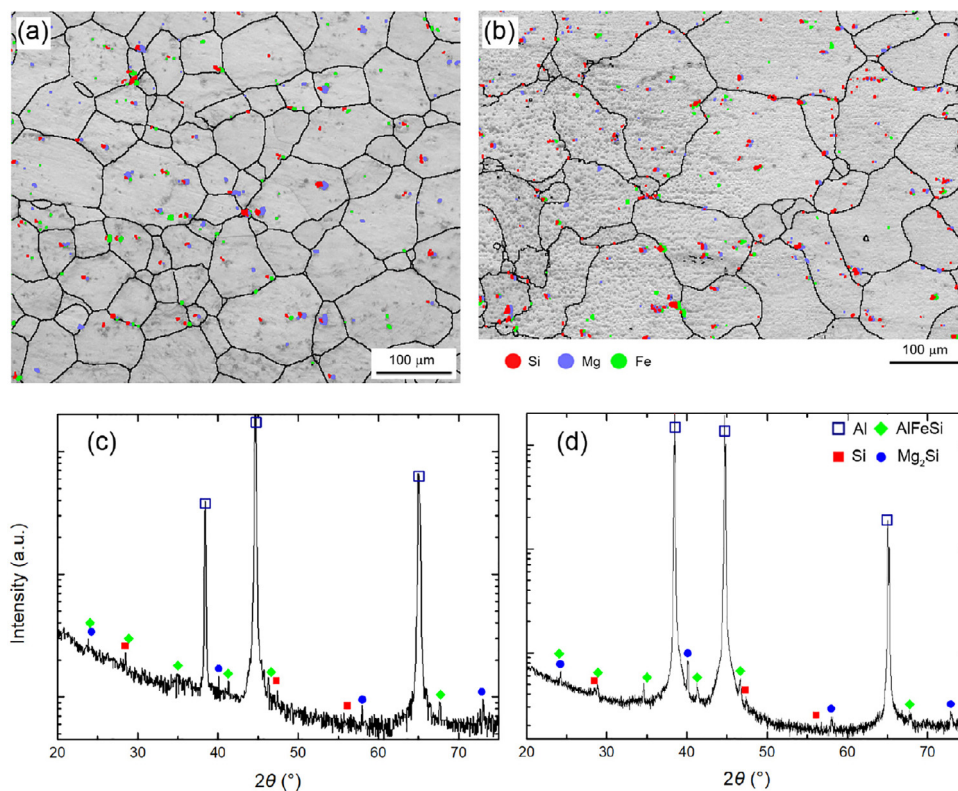
**Fig. 1.** Phase analysis of the unirradiated and irradiated LT21 Al alloy prior to tensile loading. (a) and (b) Band contrast images overlaid by element distribution mapping for the unirradiated (a) and irradiated (b) samples, respectively. The exact locations containing the minor elements (Si, Mg and Fe) are translated slightly in the horizontal direction for clarity. (c) and (d) X-ray diffraction patterns for the unirradiated (c) and irradiated (d) samples, respectively.
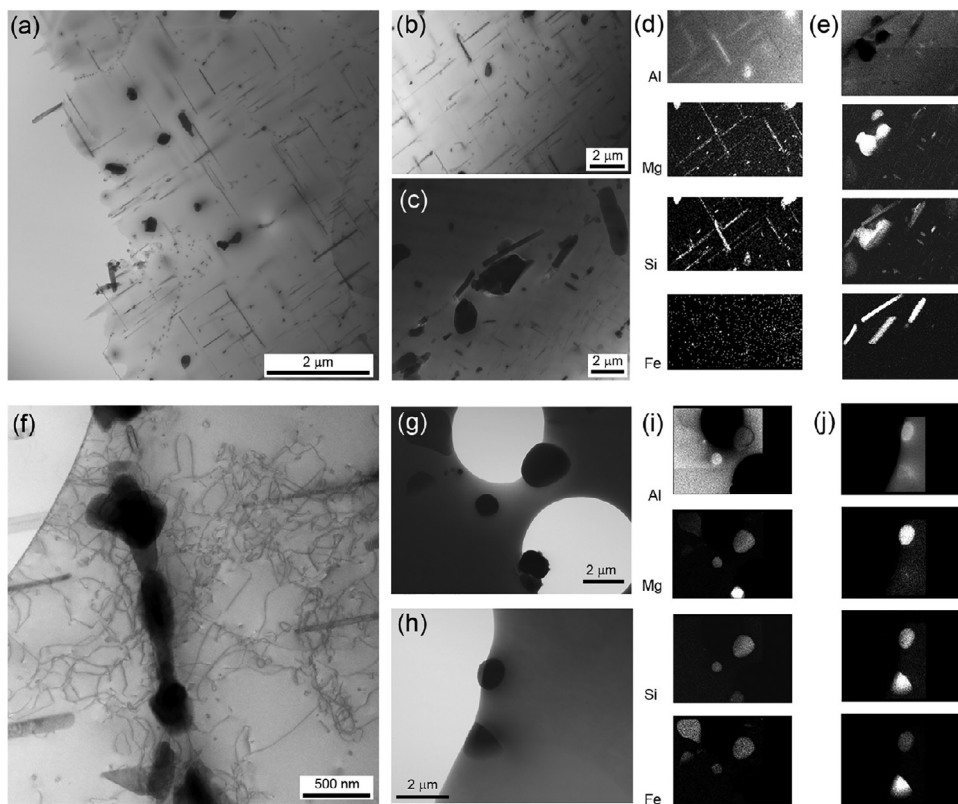


**Fig. 2.** TEM characterizations of the irradiated LT21 Al alloy prior to loading. (a), (b), (c), (f), (g) and (h) TEM images. (d), (e), (i) and (j) EDS maps corresponding to (b), (c), (g) and (h), respectively.
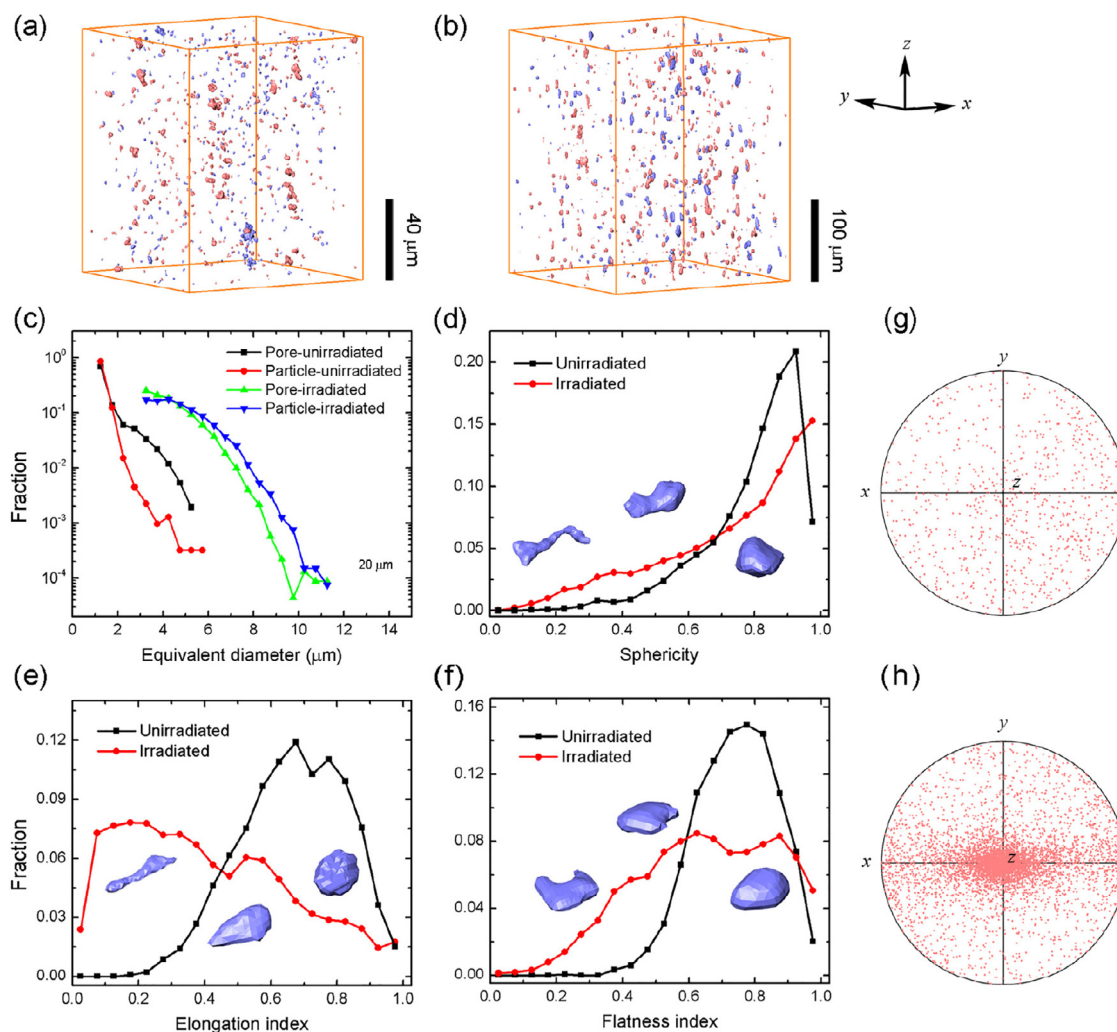
**Fig. 3.** Characterization of 3D morphologies of pores and particles in the unirradiated and irradiated LT21 Al alloy samples prior to loading. (a) and (b) Volume renderings of pores (red) and particles (blue) in the unirradiated (a) and irradiated (b) samples, respectively. (c) Equivalent diameter distributions of pores and particles. (d) Sphericity distributions of pores. (e) Elongation index distributions of pores. (f) Flatness index distributions of pores. (g) and (h) Orientation maps of the $R_1$-axes of pores in the unirradiated (g) and irradiated (h) samples, respectively. (For interpretation of the references to colour in this figure legend, the reader is referred to the web version of this article.)

the irradiated material, different from the Al alloys subjected to a similar radiation dose ($\sim 10^{21}$ n cm$^{-2}$) but at a much higher dose rate [12,19–21,23].

For 3D statistical analysis of the microstructure, synchrotron CT is applied to characterize the neutron-irradiated Al alloy, while laboratory micro-tomography (the SkyScan$^{TM}$ 2211 system) is applied to the unirradiated material for higher resolution (Fig. 3). The volume renderings of particles and pores for the unirradiated and irradiated materials are illustrated in Fig. 3a and b, respectively. The micron-sized particles and pores are distributed across the 3D matrix. The particles exhibit significantly higher absorption of X-rays than the Al matrix. Along with Fig. 3a and b, the particles in the 3D images are identified as AlFeSi. The Si and Mg$_2$Si particles have densities similar to that of the Al matrix and cannot be resolved. Therefore, AlFeSi particles are taken as an example to discuss the effects of precipitates on the mechanical behavior of neutron-irradiated LT21 Al alloy. The size or equivalent diameter distributions of the pores and particles in the unirradiated and irradiated materials are presented in Fig. 3c and d. The probability for a specific size range decreases sharply with increasing equivalent diameter for both pores and particles. The pores and particles in the irradiated material are statistically larger in size than those in the unirradiated material.

Using the GTA technique, the shape indices ($S_G$, EI and FI), and the $R_1$-axes orientation are calculated for pores in the unirradiated and irradiated materials (Fig. 3d–(f). Typical pores with specific shape indices are presented in the insets for clarity. The sphericity of pores spans widely from 0.2–1.0 (Fig. 3d). The probability in a specific $S_G$ range increases with increasing $S_G$, indicating that a considerable number of pores and particles are close to spheres. However, the sphericity of pores in the irradiated material is statistically lower than those in the unirradiated material. The EI and FI distributions of pores are presented in Fig. 3e and f, respectively. The EI distribution of pores in the irradiated material exhibits a peak at around EI = 0.2, indicating a large portion of needle-shaped pores, consistent with the EBSD and EDS results (Fig. 1). In contrast, the EI distribution of pores peaks around EI = 0.7 in the unirradiated material. Therefore, neutron irradiation leads to pronounced elongation of existing pores in the LT21 Al alloy. The FI values of pores in the unirradiated material are mostly 0.6–0.9, while those in the irradiated material exhibits a wider distribution ranging from 0.3 to 0.9. The pores become more flat or anisotropic in three dimensions. The orientation maps of the $R_1$-axes of pores in the unirradiated and irradiated materials are presented in Fig. 3g and h. The $R_1$-axes of pores are largely oriented along the $z$-axis, probably as a result of irradiation-induced anisotropy.
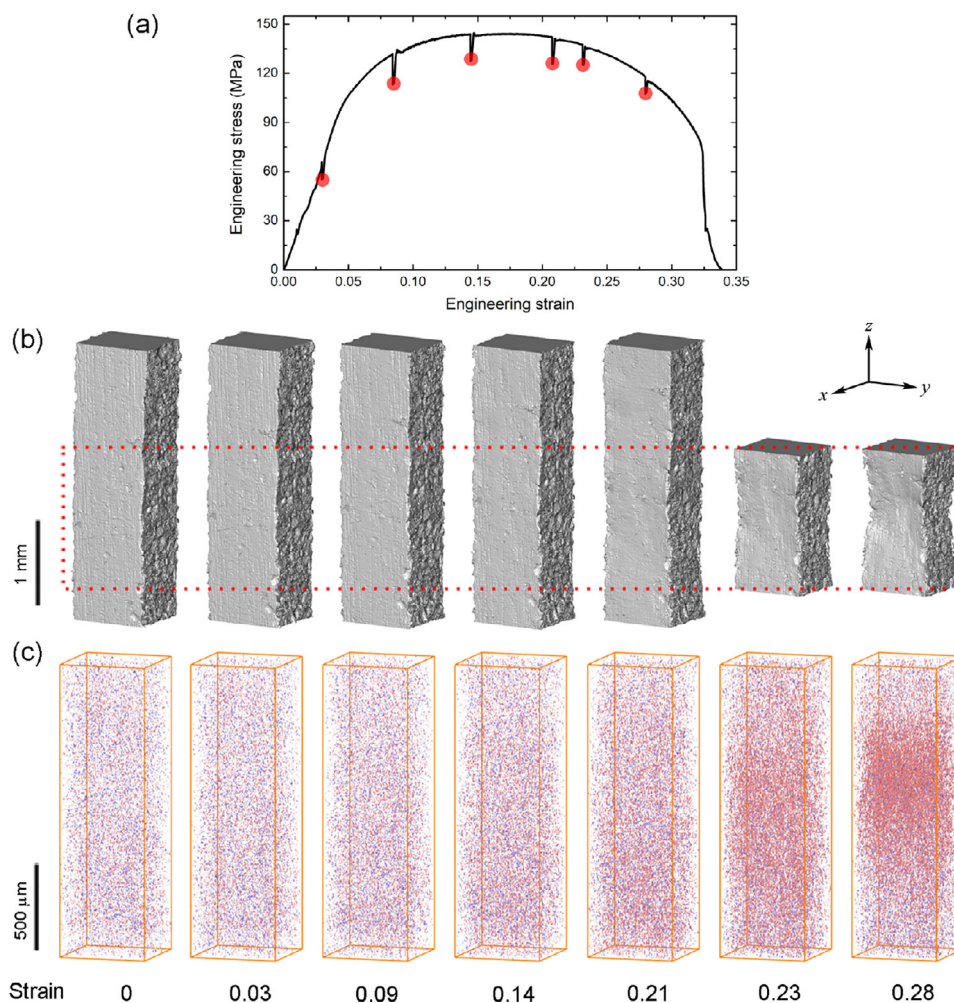
**Fig. 4.** In situ CT characterization of the irradiated LT21 Al alloy. (a) Stress–strain curve. The filled circles mark the moments for CT scans. (b) Volume renderings of the sample at different strains. (c) Corresponding volume renderings of the pores (colored red) and particles (colored blue) in the sample region marked by the dashed rectangle in (b). (For interpretation of the references to colour in this figure legend, the reader is referred to the web version of this article.)

## 3. Results and discussions

### 3.1. In situ CT results

The axial engineering stress - strain curve of the irradiated LT21 Al along with its volume renderings at seven strain levels (0–0.28) are presented in Fig. 4. The axial stress drops slightly during a CT scan. The yield strength, tensile strength and the uniform elongation are 104 MPa, 144 MPa and 0.18, respectively. Volume renderings of the sample show that the sample exhibits uniform elongation before strain 0.21 while apparent necking occurs in the sample at strain 0.23, consistent with the strain softening in the stress–strain curve. The volume renderings of the pores (red) and particles (blue) in the necking region of the sample (marked by the dashed rectangle in Fig. 4b) are illustrated in Fig. 4c. Pores and particles appear uniformly distributed across the sample at the initial state. Then the volume of pores increases gradually with increasing loading. After strain 0.21, the density and volume of pores in the necking region increase significantly and leads to tensile failure of the sample.

Displacement vectors (**u**) of particles and strain fields $\varepsilon_{zz}(x, y, z)$ across the sample throughout its deformation process are obtained via PTV. At least 80% of the particles in the sample are successfully tracked for all loading steps. The "missing" particles are distributed randomly across the sample, instead of being localized into specific

regions, and thus, the statistical reliability of PTA can be assured [44]. Correlation is carried out between tomograms at two adjacent strain levels. Figure 5a shows the displacement vector maps across the sample. The displacement gradient across the sample increases with increasing loading. Figure 5b shows the strain fields at different bulk strains. They are approximately uniform across the sample before strain 0.09. Local strain localizations occur in the sample at strain 0.14, as marked by the arrows on the exposed surfaces. They are probably resulted from local microstructural heterogeneities (e.g., pores and particles). The strain localization on the lower part of the sample grows in amplitude and area at strain 0.21, which forms two shear deformation bands as guided by the dashed lines. This area corresponds to the necking region at strain 0.23. Necking appears to occur earlier as indicated by the strain fields than by the 3D images of sample (Fig. 4b). The strain fields indicate that the sample fails via tension-induced shear.

### 3.2. Porosity evolution

To demonstrate the evolution of pores more clearly, 3D images of pores and particles in the same local region at different strains are tracked by the PTA and presented in Fig. 6. The pore structure changes little at strain 0.03. Above this strain, growth and coalescence of initial pores and formation of "new" pores are both observed in the sample. Here, "new" is defined on the basis of the CT
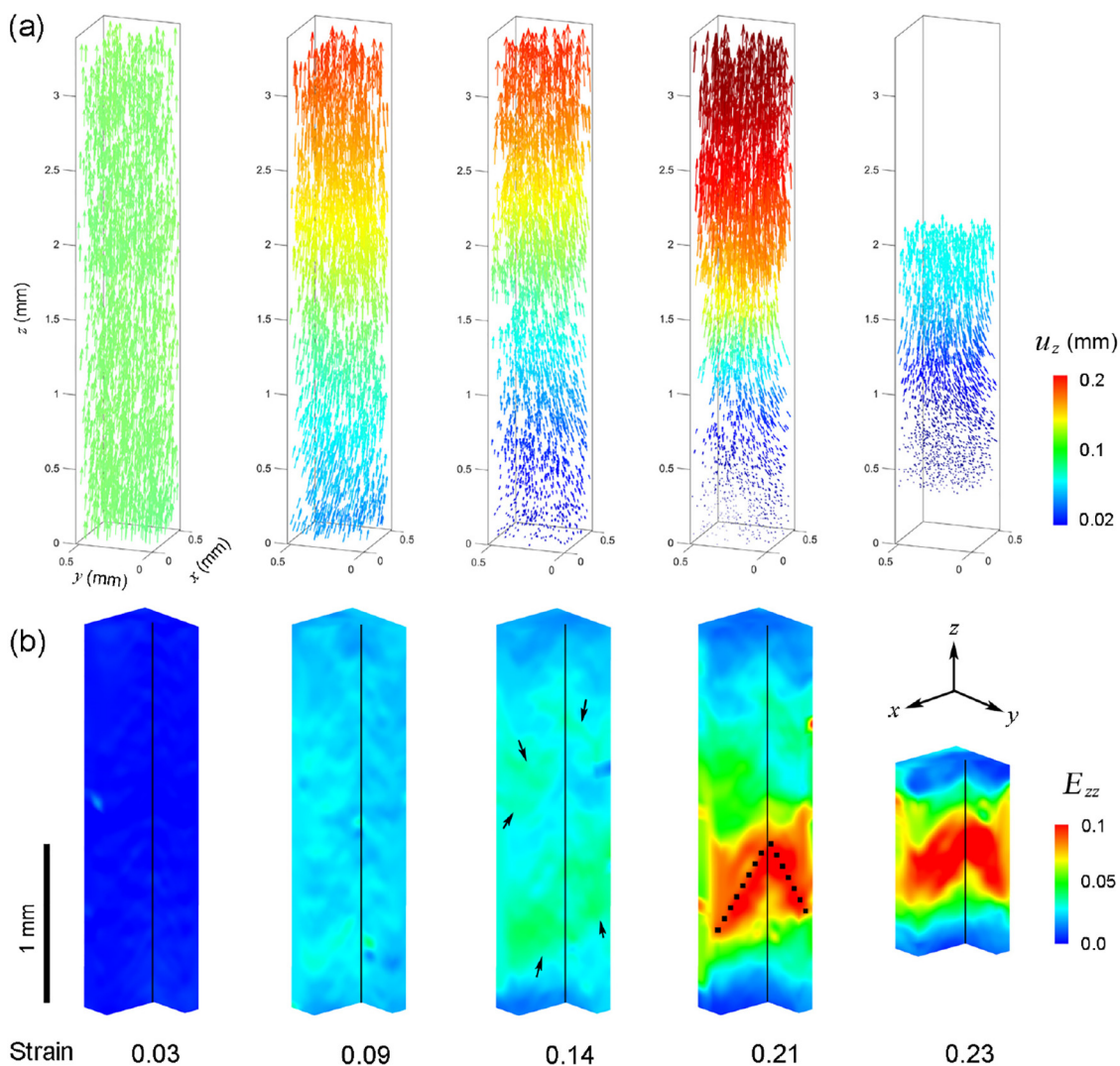
**Fig. 5.** (a) Displacement vectors (**u**) of particles and (b) strain fields (the $z$-component $\varepsilon_{zz}$) at different bulk strains as noted, quantified via PTA.

resolution. Formation of "new" pores is actually resulted from the growth of existed pores below 3 μm and/or nucleation and growth of new pores. The pores around particles are prone to grow earlier and faster, probably due to strain mismatch between particle and matrix. For instance, there exist two pores at the upper and lower ends of particle A before loading. These two pores exhibit pronounced growth at strain 0.09 (marked by the dashed rectangle) and coalesce with a nearby pore. They continue to grow in the axial and lateral directions. Similar pore growth is observed around particles B and D at strain 0.03 (marked by the arrows). The pores with no Fe-based particles around (or particles not detected) also grow during tension, e.g., pores E and F. Pore E grows significantly and coalesces with a pore nearby at strain 0.09 (marked by the dashed ellipse). Apart from the pore growth, formation of pores is observed to occur at the particle-matrix interface region. This can be seen clearly for particles B and C. At strain 0.09, a small pore appears at the upper end of particle B (marked by the vertical arrow) and the lower right end of particle C, respectively. Then, the new pores grow continually with increasing strain, but grow more slowly than those initial pores around particles. Another pore appears at the lower end of particle B at strain 0.21. Formation of pores also occurs in the region without Fe-based particles (marked by the arrows at strain 0.23). The particles stay nearly unchanged throughout the deformation process.

The porosity distributions along the sample height at different strains are presented in Fig. 7a. The porosity distribution is uniform along the sample height before strain 0.14. After that, the porosity at the lower part of the sample (0.7–1.7 mm segment) increases faster than those at the other parts, mainly due to the rapid growth of pores in the necking region. The porosity distribution changes from a uniform distribution to a bell-shaped one. The peak porosity at the height 1.2 mm reaches 1.6%, 2.5 times the overall porosity. To quantify the morphology evolution of pores, the size and shape indices of pores across the sample are calculated using the GTA technique throughout the deformation process. The statistical analysis above 0.14 strain is conducted in the necking region (0.6–1.8 mm height). The equivalent diameter distributions of pores at different strains are shown in Fig. 7b. The fraction of pores in a specific diameter range decreases approximately exponentially with increasing equivalent diameter. The equivalent diameter distribution of pores remains approximately constant below strain 0.09 and shifts gradually to the large diameter direction after that. The mean equivalent diameter of pores increases from 4.3 μm at the initial state to 5.1 μm at strain 0.28. The sphericity distribution of pores varies little during loading, and not presented for brevity. The EI and FI distributions show more pronounced changes. With increasing loading, the fraction of pores with EI = 0–0.2 increases, while that for EI = 0.2–0.6 decreases (marked by
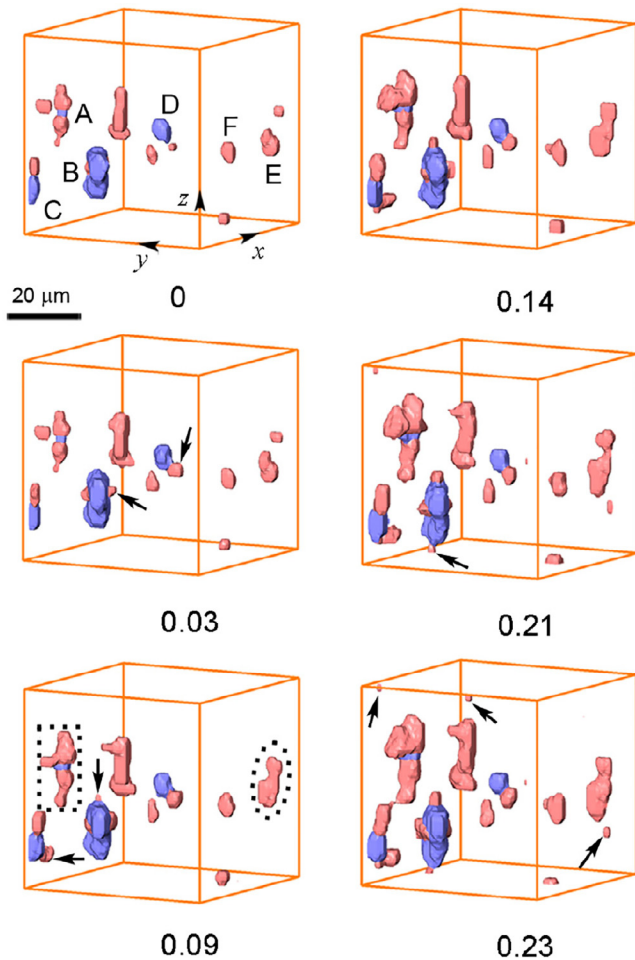
**Fig. 6.** Snapshots of particles (colored blue) and pores (colored red) in a selected volume tracked via PTA at different bulk strains as noted. (For interpretation of the references to colour in this figure legend, the reader is referred to the web version of this article.)

the arrows, Fig. 7c). This indicates elongation of pores along the tensile direction during loading. As for the FI distribution (Fig. 7d), the fraction for FI = 0.2–0.6 decreases, while that for FI = 0.6–0.8 increases, with increasing loading (marked by the arrows, Fig. 7d). The increase in FI indicates that the pores become more circular in the sample cross-section perpendicular to the loading direction.

### 3.3. Formation of pores

To discuss the characteristics of pore formation within the CT resolution, the distance between the barycenter of a pore to that of its nearest neighbor particle, $L_b$, is calculated for all such pores. The number distribution of $L_b$ is presented in Fig. 8a. The number is normalized by the volume of CT field of views. The distribution curve exhibits two peaks at about $L_b = 4.5$ $\mu$m and $L_b = 20$ $\mu$m. Since the mean equivalent diameter of pores and particles are 4.7 $\mu$m and 4.3 $\mu$m, the first peak supposedly corresponds to tension-induced pore formation at the particle-matrix interfaces. This peak is much narrower than the second one at $L_b = 20$ $\mu$m. The first peak value increases significantly with increasing strain (marked by the red shadow), implying that more and more pores are formed at the particle-matrix interfaces. The second peak may correspond to random pore formation across the sample. $L_b$ at the second peak is determined by the particle number density in the sample. In addition, the first peak exists in the sample prior to loading, consistent with the CT images that pore appear around

particles in the initial sample (Fig. 6). Therefore, neutron irradiation can induce pore formation and growth at the particle-matrix interfaces as well.

Figure 8a is further processed to calculate the probability density distribution of $L_b$ for newly-formed pores at different strains (Fig. 8b). Assuming that $L_b$ of existed pores keeps approximately constant between adjacent deformation stages, the probability density for $L_b$ for newly-formed pores at the $i$th deformation stage, denoted as $f_i(L_b)$, is calculated as

$$f_i(L_b) = \frac{\sum_{L_b-\delta}^{L_b+\delta} M_i(\hat{L}_b) - \sum_{L_b-\delta}^{L_b+\delta} M_{i-1}(\hat{L}_b)}{2\delta(N_{b,i} - N_{b,i-1})}, \tag{3}$$

where $M_i(\hat{L}_b)$ and $M_{i-1}(\hat{L}_b)$ are the numbers of $\hat{L}_b$ at the $i$th ($i =$ 2–7) and $(i-1)$th deformation stages, respectively. $\delta$ is half statistical interval length and is 0.5 $\mu$m here. $N_{b,i}$ or $N_{b,i-1}$ is the total number of pores at the $i$th or $(i-1)$th deformation stage.

The probability density distribution at strain 0.03 shows some oscillations due to the small number of pores formed. The distribution curves at strains 0.09, 0.14 and 0.21 are similar, and show two peaks as well. The distribution curves at larger strains (0.23 and 0.28) becomes different from those at lower strains. The first peak becomes significantly higher while the second peak shifts slightly to the low $L_b$ direction, due to a pronounced increase in pore density in the necking region. Consistently, the probability density becomes negative in the range of $L_b = 25$–45 $\mu$m.

The bimodal distribution curves during the middle three deformation stages (strains 0.09–0.21) are attributed to two modes of pore formation, i.e, at the particle-matrix interfaces (mode I) and randomly formed across the sample (mode II). For simplicity, pores with $L_b \leq 9$ $\mu$m are denoted as mode I while pores with $L_b > 9$ $\mu$m, mode II. For the random formation of pores across the sample, a model can be constructed according to the probability theory. For a multiple-particle system, suppose that random formation of a single pore outside a spherical region of radius $L_b$ of each particle is an independent event. Then, the cumulative probability of random pore formation inside a spherical region of radius $L_b$ can be described according to the multiplication rule as

$$G_{II}(L_b) = 1 - \lim_{V_s \to +\infty} \left(1 - \frac{4\pi L_b^3}{3V_s}\right)^{V_s\rho_a}, \tag{4}$$

where $V_s$ is the sample volume and can be considered as infinitely large compared to the pore volume (by three orders of magnitude), and $\rho_a$ is the volume density of particles. $1 - 4\pi L_b^3/3V_s$ is actually the probability for a single pore randomly formed outside a spherical region of radius $L_b$ of a single particle. The probability density of pore formation via mode II is derived from Eq. (4) as

$$g_{II} = P_{II}4\pi \rho_a L_b^2 \exp\left(-\frac{4}{3}\pi \rho_a L_b^3\right), \tag{5}$$

where $P_{II}$ refers to the total probability of pore formation via mode II.

The pore formation model is applied to fit the experimental data (Fig. 8c). The parameters fitted from the data are $P_{II} = 83.2\%$ and $\rho_a = 2.23 \times 10^{-5}$ $\mu$m$^{-3}$. The model describes the second peak of the experimental data, confirming that the second peak is resulted from random formation of pores across the sample. The ratio between the total volume and volume growth of pores associated to mode I and mode II in each deformation stage are calculated and presented in Fig. 8d). The total volume and volume growth of pores in mode I are significantly lower than those in mode II, but increases with increasing loading. Nevertheless, the density of pores formed via mode I is considerably higher than that via mode II.

Pores tend to appear adjacent to particles. To clarify the relative position between particles and pores, the azimuthal angles for
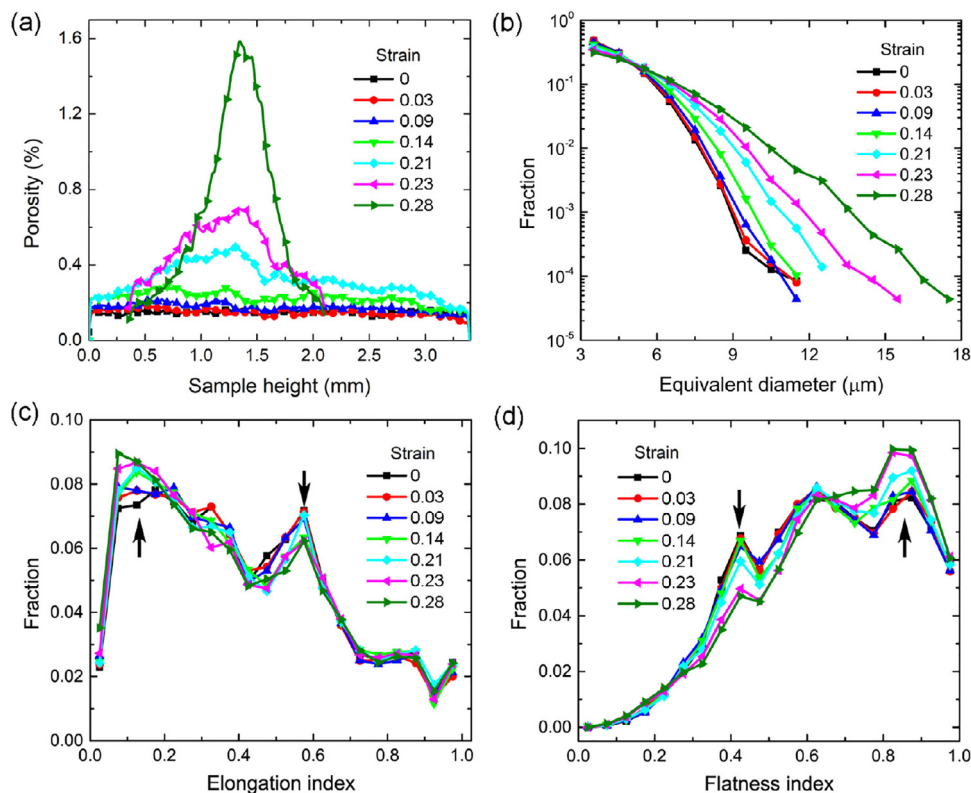
**Fig. 7.** 3D characterization of pores at different strains. (a) The porosity distribution along the sample height. (b) Equivalent diameter distribution. (c) Elongation index distribution. (d) Flatness index distribution.
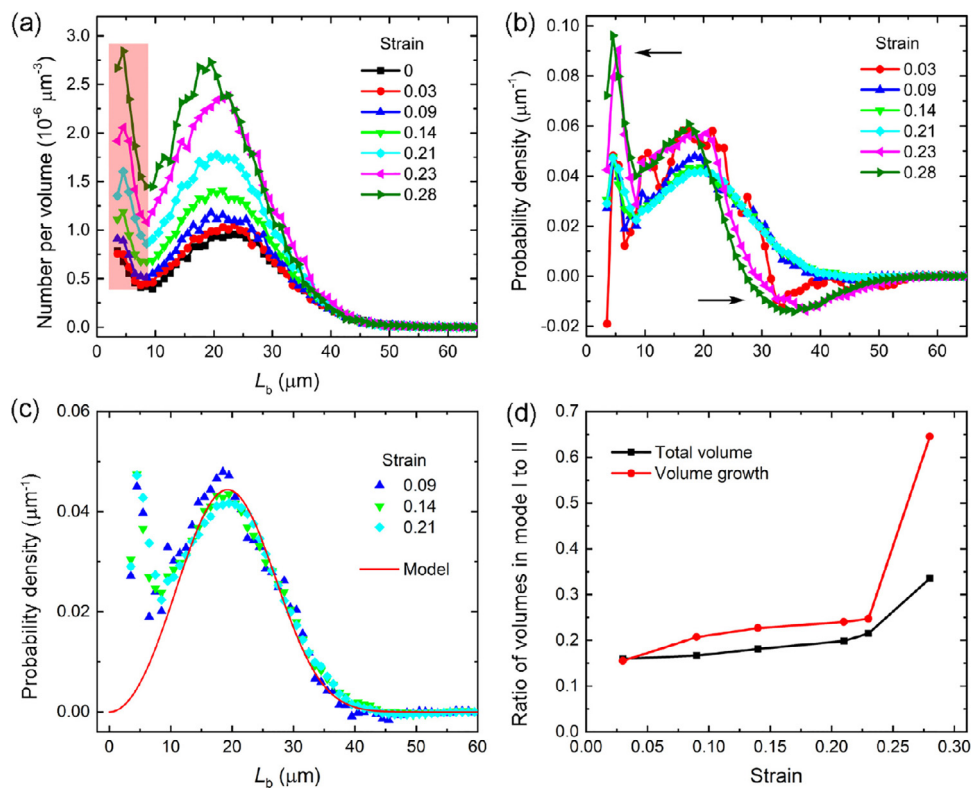


**Fig. 8.** Quantification of the pore formation modes at different strains. $L_b$ is the distance between the barycenters of a pore and its nearest-neighbor particle. (a) Number per volume distribution of $L_b$ for all pores at different strains (corresponding to Fig. 4b). (b) Probability density distribution of $L_b$ for newly nucleated pores (excluding the initial pores). (c) Comparison of pore formation probabilities between the experimental results (symbols) and the model prediction (the dashed line). (d) The ratio between the volumes of pores in mode I and mode II regions, and the ratio between the volume growths associated to modes I and II in each stage.
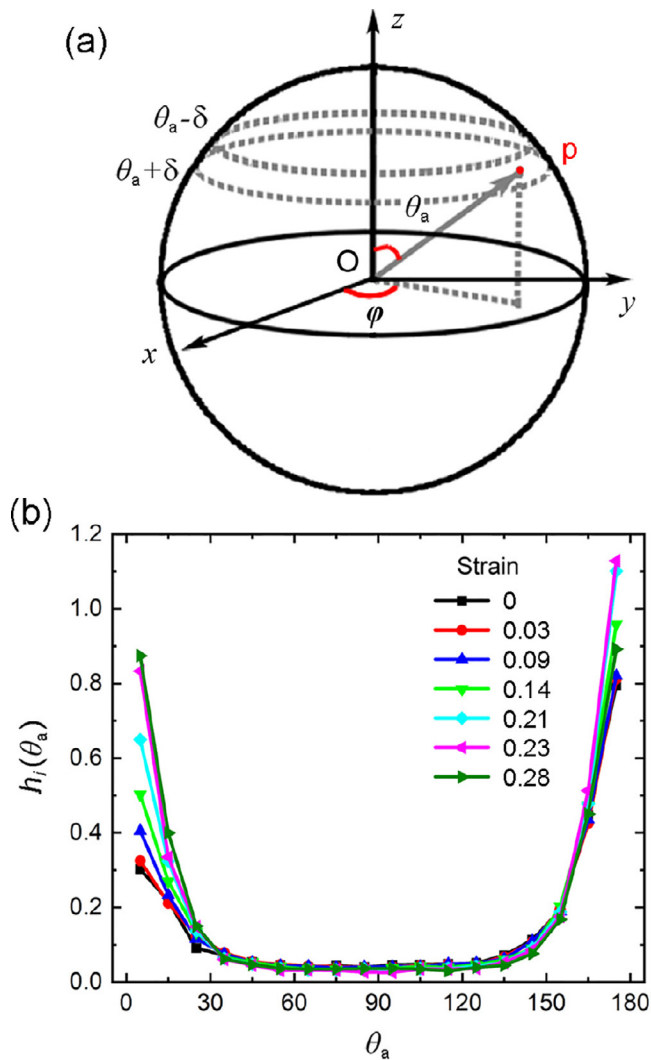
**Fig. 9.** (a) Geometry for pore formation on a particle surface. Point p and point O refer to the barycenters of pore and particle, respectively. $\theta_a$ and $\phi$ are azimuthal angles. (b) Probability density distribution $h(\theta_a)$ as a function of $\theta_a$ (Eq. (6)).

particle-pore pairs are quantified. The geometry between each particle and its neighboring pores with a center-of-mass distance less than 9 $\mu$m is illustrated in Fig. 9a. The barycenters of the pore and particle are marked as point p and point O, respectively. The angle between segment pO and the $z$-axis is $\theta_a$. The probability density distribution corrected by weighted average of $\theta_a$, $h_i(\theta_a)$, can be calculated as

$$h_i(\theta_a) = \frac{\sum_{\theta_a-\delta}^{\theta_a+\delta} S_i(\hat{\theta}_a)}{2\pi N_{a,i}[\cos(\theta_a - \delta) - \cos(\theta_a + \delta)]}, \tag{6}$$

where $S_i(\hat{\theta}_a)$ is the number of $\hat{\theta}_a$ at the $i$th ($i = 1$–7) deformation stage. $\delta$ is half statistical interval length and is 5° here. $N_{a,i}$ is the total number of particles at the $i$th deformation stage. The weight factor $2\pi[\cos(\theta_a - \delta) - \cos(\theta_a + \delta)]$ represents the solid angle of the ring region from $\theta_a - \delta$ to $\theta_a + \delta$ in Fig. 9a.

The $h_i(\theta_a)$ curves (Fig. 9c) are U-shaped, and flat (close to zero) in the 30°–150° range. In contrast, the two ends of the curves both exhibit a pronounced increase with increasing loading, indicating that the pores are prone to form at the upper and lower ends of particles. This is consistent with the numerical modelling results in particle-reinforced composites under uniaxial tension [45,46]: decohesion and cracking tend to occur at interfaces perpendicular to the tensile direction, due to higher tensile stress there. The

particle-pore interactions for AlFeSi are expected also applicable to other types of particles (Si and Mg$_2$Si) in LT21 Al, and may be partly extended to particle-reinforced metal composites.

### 3.4. Growth of pores

To quantify the growth of (initially existed and newly formed) pores within the CT resolution, the displacement fields (Fig. 5a) are used to track the pores between adjacent (reference and current) tomograms. First of all, the position of each pore in the reference tomogram is updated with the displacement vectors of neighbor particles, via triangulation-based natural neighbor interpolation and nearest neighbor interpolation. Then correlation analysis is carried out between the updated reference tomogram and the current tomogram. With the consideration of the large variation in pore shape and volume, the shape term and the volume term in Eq. (A.1) can be removed, and the similarity between pores is judged by the position criterion,

$$C_d = K \exp\left(-\frac{1}{\sigma_g}\sqrt{\sum_\alpha \frac{\Delta x_\alpha^2}{\sigma_\alpha}}\right). \tag{7}$$

Here $C_d$ is essentially the first term in Eq. (A.1) and all the variables are defined in Eq. (A.1). The weight factors are expressed as $\sigma_1 = \sigma_2 = \sigma_3 = 1$; $\sigma_g$ is chosen to be 10 $\mu$m to confine the search to the vicinity of the predicted position. The threshold for $C_d$ is chosen empirically as 0.91 for the best match. Iterative outlier removal is performed to eliminate erroneous tracking.

The volumes of pore $k$ at the $i$th and $(i-1)$th deformation stages are labeled as $V_{b,i}^{(k)}$ and $V_{b,i-1}^{(k)}$, respectively. The ratio of $V_{b,i-1}^{(k)}$ to $V_{b,i}^{(k)}$ quantifies the growth of pore $k$ between two adjacent deformation stages. The mean growth ratio of pores at a specific sample height, $z$, is calculated as

$$\psi_i(z) = \frac{1}{Q_{b,i}} \sum_{k=1}^{Q_{b,i}} \frac{V_{b,i}^{(k)}}{V_{b,i-1}^{(k)}}, \tag{8}$$

where $Q_{b,i}$ is the number of tracked pores located at the sample height $z$ from the $(i-1)$th to $i$th deformation stages. To obtain representative and reliable results, the particles in a 50 $\mu$m thick neighborhood centered at $z$ is used for average and calculation. The distributions of $\psi_i$ along the sample height at different strains are presented in Fig. 10a. At strain 0.03, the growth ratio is close to 1.0 across the sample. At strains 0.09 and 0.14, it exhibits an overall increase and is approximately uniform across the sample. The mean growth ratio is about 7% (strain 0.09) and 13% (strain 0.14), respectively. After that, the pore volume increases significantly at the necking region of sample. The maximum growth ratio reaches 65% at strain 0.23.

The normalized porosity increase, $\eta_i$, in the sample at the $i$th deformation stage is calculated as

$$\eta_i = \frac{V_{b,i} - V_{b,1}}{V_{b,7} - V_{b,1}}, \tag{9}$$

where $V_{b,i}$ ($i = 1$–7) is the total volume of pores in the necking region at the $i$th deformation stage. For each deformation stage, this region is taken as a 500-$\mu$m-wide region with its center marked by black dots in Fig. 10a. With increasing loading, $\eta_i$ (Fig. 10b) increases slightly before strain 0.14, but rapidly to 1.0 after that.

As discussed in Section 3.3, the porosity increase in the sample comes from both formation of new pores and growth of initial and nucleated pores. It is natural to ask how these two factors contribute to the porosity increase in the irradiated sample. Since not all pores are tracked throughout the loading process, the increase in pore volume due to pore growth is difficult to calculate directly. The growth ratio of all pores is estimated by that of the tracked
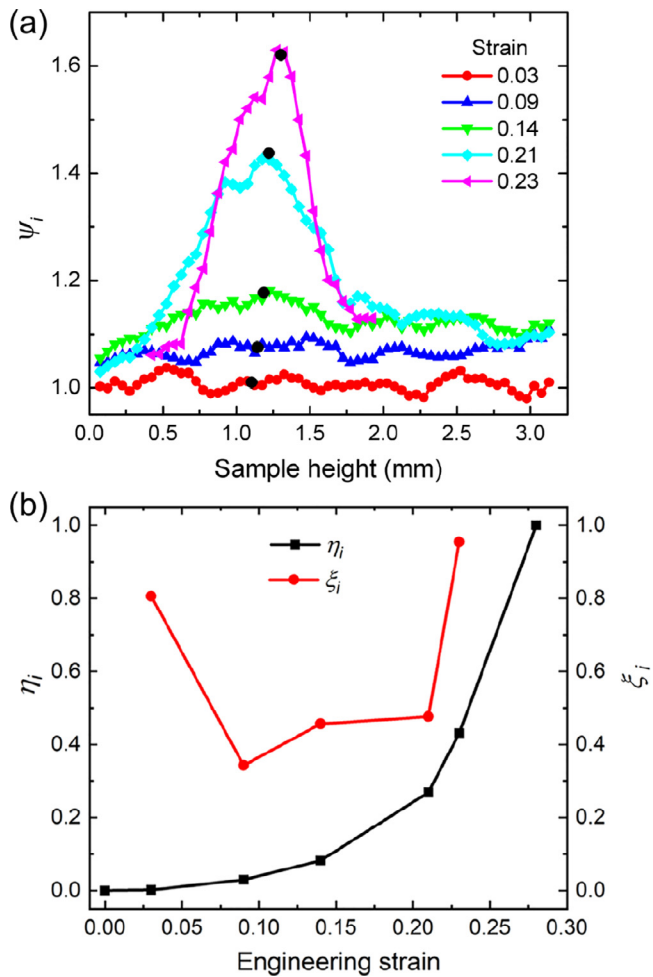
**Fig. 10.** (a) The mean growth ratio ($\psi_i$) of pores as a function of sample height for different bulk strains. (b) Evolution of the normalized porosity increase ($\eta$) and the contributing fraction ($\xi_i$) of pore growth to this increase with the bulk strain.

pores (randomly sampled from the pore assembly). The contribution of pore growth to the porosity increase can be quantified by $\xi_i$, defined as

$$\xi_i = \frac{\sum_{z=z_{n,i}}^{z_{p,i}} (\psi_i(z) - 1) V_{b,i-1}(z)}{V_{b,i} - V_{b,i-1}}, \qquad (10)$$

where $V_{b,i}(z)$ refers to the total volume of pores in a 50 $\mu$m thick neighborhood centered at the sample height $z$ at the $i$th deformation stage, in accordance with the calculation of $\psi_i(z)$ (Eq. (8)). $z_{p,i}$ and $z_{n,i}$ represent the height at the upper and lower boundaries of the necking region at the $i$th deformation stage, respectively. Evolution of $\xi_i$ with bulk strain is presented in Fig. 10b. $\xi_i$ is about 0.81 at strain 0.03, decreases to 0.35–0.45 during strains 0.09–0.21 and increases again to ~0.95 after necking. Therefore, pore formation contributes equally or more to porosity or damage accumulation in the sample during stable plastic deformation, compared to pore growth. The initial pores do not grow quickly or coalesce into micro cracks until necking occurs (Fig. 6), contrary to pores in conventional porous metals [47,48].

To reveal the effects of grain boundaries on the local plastic deformation of the irradiated material, the irradiated sample after tension to 0.09 strain is characterized with EBSD and EDS (Fig. 11). Figure 11a and b shows the kernel average misorientation (KAM) map of the postmortem sample. The tensile direction is along the horizontal direction. The KAM map shows a heterogeneous local distribution of KAM values. Dot-shaped high-KAM-value areas ap-
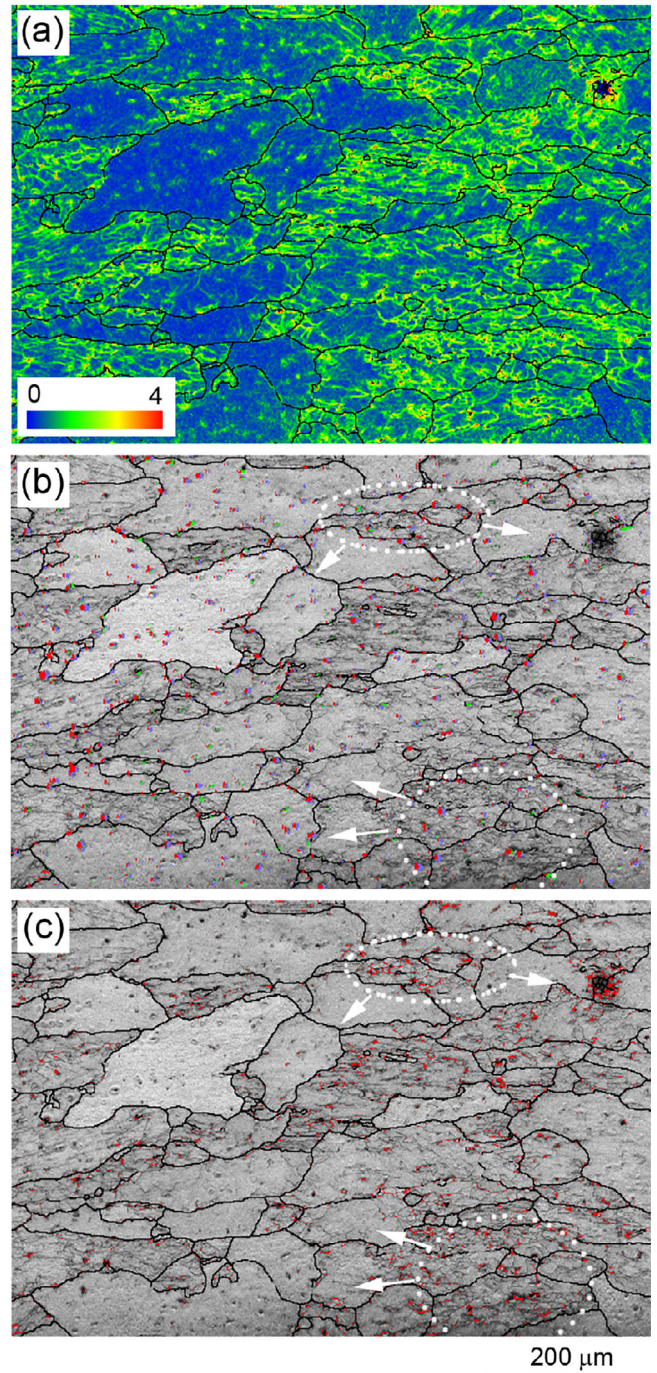


**Fig. 11.** EBSD and EDS characterizations of the irradiated sample after tension to 9% strain. (a) KAM map. (b) Band contrast image overlaid by element distribution mapping (red for Si, blue for Mg and green for Fe). The exact locations of minor elements are translated slightly in the horizontal direction for clarity. (c) Band contrast image overlaid by distribution map of KAM values greater than 2.5 (red dots). (For interpretation of the references to colour in this figure legend, the reader is referred to the web version of this article.)

pear across the sample, while zero KAM-value areas appear in some of the grains. The element distribution maps for Si, Mg, and Fe are overlaid on the band contrast map of the Al matrix. Meanwhile, the pixels with KAM values greater than 2.5 are extracted and colored red as shown in Fig. 11c. The distributions of particles and high-KAM-value localities show spatial correlations. The regions with high density particles exhibit high KAM values as well, as marked by the dotted ellipses. However, those grains contain-

ing few particles (marked by the arrows) show approximately zero KAM values. Therefore, the particles tend to induce strain localizations around them, while grain boundaries show less influence on the local plastic deformation.

## 4. Conclusions

EBSD, EDS, TEM and micro CT are applied to characterize the microstructures of the LT21 Al alloys aged naturally and in service in a neutron reactor for 30 years. Quasi-static uniaxial tensile tests are carried out on the LT21 Al alloy from the decommissioned reactor. *In situ* synchrotron micro CT is adopted to characterize the deformation and damage dynamics of this LT21 Al alloy. A particle tracking analysis technique is developed to quantify the displacement/strain fields and microstructural evolution (e.g., particle movement and pore growth) in the irradiated sample. The main conclusions are summarized as follows.

- Long-term neutron irradiation in the temperature range of 20 - 40°C induces considerable microstructural changes in the LT21 Al alloy. Nanoscale needle-shaped $Mg_2Si$ particles appear in the irradiated material. The shape of AlFeSi particles are largely needle-shaped in the irradiated material, but are largely plate-shaped in the unirradiated material. In addition, the size of pores and particles in the irradiated material becomes larger than that in the unirradiated material. The shape of pores becomes more anisotropic after irradiation.
- The alloy undergoes elastic-plastic deformation followed by shear-dominated necking failure. The porosity and pore size exhibits an overall increase with increasing loading. The aspect ratio of pores change slightly, as a result of formation of spheroidal pores and elongation of pre-existing pores along the tensile direction.
- During tension, formation of new pores (judged on the CT resolution level) occurs in two modes: (I) formation at the particle-matrix interface, and (II) random formation across the sample. The spatial distribution of pores in mode II follows a random formation model. For mode I, pores tend to form at the top and bottom ends of a particle (along the loading direction), due to strain-mismatch at the particle-matrix interfaces.
- Before necking occurs, formation of new pores and growth of initial and newly-formed pores occur simultaneously and contributes approximately equally to damage accumulation in the irradiated material.

## Data availability

The raw data related to this manuscript would be made available on request.

## Declaration of Competing Interest

The authors declare that they have no known competing financial interests or personal relationships that could have appeared to influence the work reported in this paper.

## Acknowledgments

## Appendix A. Particle tracking analysis

To map the local deformation of the Al matrix, the particles are tracked via 3D correlation analysis between the reference and current tomograms. The key parameter for PTA is the correlation parameter ($C$) used to evaluate the similarity between two particles in the reference and current tomograms,

$$C = K \exp\left(-\frac{1}{\sigma_g}\sqrt{\sum_\alpha \frac{\Delta x_\alpha^2}{\sigma_\alpha}}\right) \cdot \frac{\overline{V} - |\Delta V|}{\overline{V}} \cdot \frac{3\sum_{\alpha>\beta}\lambda_\alpha\lambda_\beta}{(\sum_\alpha\lambda_\alpha)^2}, \quad (A.1)$$

in terms of position, volume and shape, respectively (three terms on the right-hand side of Eq. (A.1)). Here, $\Delta x_\alpha = x_\alpha^{(n)} - x_\alpha^{(m)}$, and three $x_\alpha$ values are the barycenter coordinates of a particle; $\alpha = 1, 2, 3$ corresponds to the $x$-,$y$- and $z$-axes, respectively. Superscripts $m$ and $n$ refer to the particle indices in the reference and current particle lists, respectively. $K = (1 + |\Delta z|/\Delta z)/2$ is used to eliminate particles moving along the negative $z$-axes. $\sigma_\alpha$ and $\sigma_g$ are weight factors, and $\sigma_1 = \sigma_2 = 1$. $\Delta V_a = V_a^{(n)} - V_a^{(m)}$, and $\overline{V}_a = (V_a^{(m)} + V_a^{(n)})/2$, where $V_a$ refers to particle volume. $\lambda_\alpha = \left(R_\alpha^{(n)}/R_\alpha^{(m)}\right)^{1/2}$.

The flow chart for PTA is illustrated in Fig. A1a. For a specific particle $m$ in the reference tomogram, correlation analysis I is conducted between particle $m$ and each particle in the current tomogram, $n$. The weight factors $\sigma_3$ and $\sigma_g$ are set as 100 and 1000 μm, respectively. The $C$ values for all particle pairs are sorted. If the largest $C$ value exceeds 0.9 (otherwise an invalid correlation), particle $n$ yielding the largest $C$ is considered the best match for particle $m$ after movement. The displacement vector between particles $m$ and $n$ is calculated. The correlation-calculation process is repeated for all the particles in the reference tomogram, and a collection of displacement vectors are obtained. Then, an iterative outlier removal algorithm is proposed to remove erroneous displacement vectors. The basic principle is that a correct displacement vector for a particle should be similar to those for its neighbors in amplitude and orientation. For particles with poor correlation, their displacement vectors are derived from the neighboring correct displacement vectors via interpolation. The coordinates of particles in the reference tomogram are updated. After that, iterative correlation analysis II is carried out between particles in the updated reference tomogram and current tomogram. Each correlation analysis is followed by iterative outlier removal. The single correlation-calculation process is similar to that in correlation analysis I. The weight factors $\sigma_3$ and $\sigma_g$ are set as 1 and 10 μm, respectively. Correlation and iterative outlier removal are applied alternately until a satisfactorily refined displacement field is obtained.

After correlation analyses I and II, triangulation-based natural neighbor interpolation [49] is used to derive the displacement field from the displacement vectors of particles. A low-pass convolution filter [50] is applied to the displacement field which provides higher instability damping at the expense of spatial resolution. The Lagrangian–Green normal and shear strains are calculated from displacement (**u**) gradients. The central difference method is used to calculate the partial differential or gradient of the displacement field. For boundary voxels, a single-sided difference method is adopted instead of the central difference method.

To evaluate the performance of PTA, a virtual displacement field is imposed onto a 3D gray-scale image [51]. The displacement field **u** follows a 3D Gaussian distribution: $\mathbf{u} = (0, 0, u_z)$; $u_z(x, y, z) = 50 - 50\cos(2\pi z/1000)$ μm, where $x, y, z$ are the coordinates of a voxel. Details on the displacement imposing process can be found elsewhere [34]. After that, the particles are extracted from the 3D image for PTA. To test the anti-interference capability of PTA, a number (10% of total) of noise particles are added to the initial and deformed images. The PTA results show that 98% of the real particles are accurately tracked. The predefined and calculated displacement fields are compared in Fig. A1b, and agree well with each other. The precision [51] for displacement calculation is 0.41 μm.
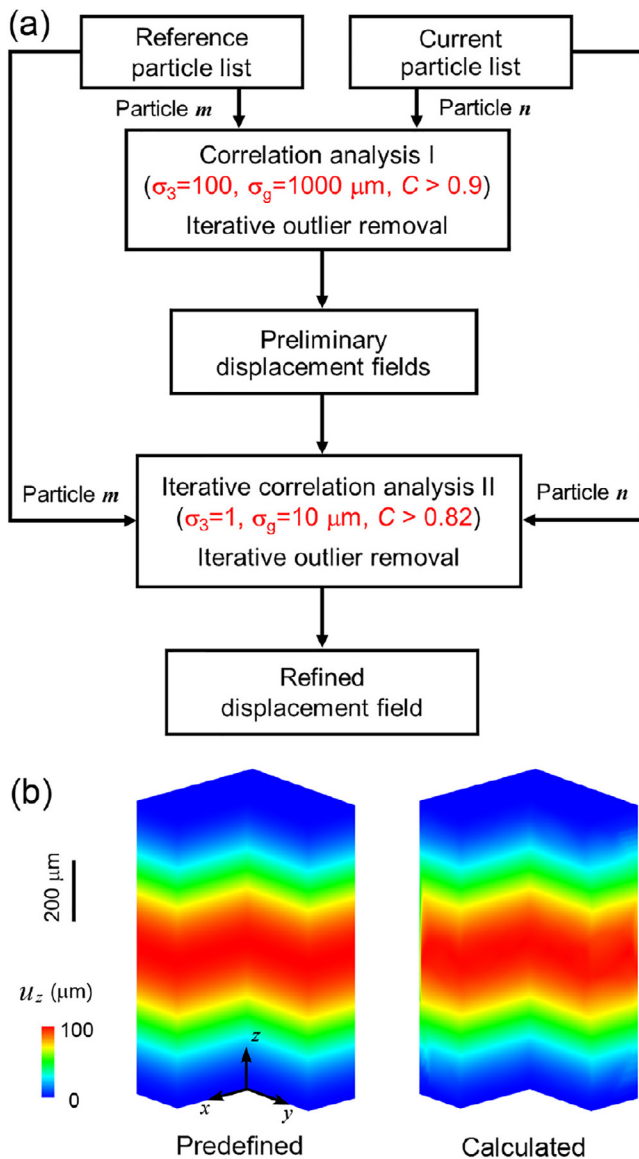
**Fig. A1.** Flow chart for the particle tracking analysis (PTA). $\sigma_3$ and $\sigma_g$ are correlation parameters defined in Eq. (A.1), while $C$ is correlation coefficient defined in Eq. (A.1).

## References

[1] K. Farrell, J. Bentley, D.N. Braski, Direct observation of radiation-induced coated cavities, Scr. Metall. 11 (3) (1977) 243–248.

[2] S.J. Zinkle, G.S. Was, Materials challenges in nuclear energy, Acta Mater. 61 (3) (2013) 735–758.

[3] W. Xu, Y. Zhang, G. Cheng, W. Jian, P.C. Millett, C.C. Koch, S.N. Mathaudhu, Y. Zhu, In-situ atomic-scale observation of irradiation-induced void formation, Nat. Commun. 4 (1) (2013) 1–6.

[4] D. Liu, B. Gludovatz, H.S. Barnard, M. Kuball, R.O. Ritchie, Damage tolerance of nuclear graphite at elevated temperatures, Nat. Commun. 8 (1) (2017) 1–9.

[5] Y. Lu, Q. Shao, H. Yue, F. Yang, A review of the space environment effects on spacecraft in different orbits, IEEE Access 7 (2019) 93473–93488.

[6] R.W. Hamm, M.E. Hamm, The beam business: Accelerators in industry, Phys. Today 64 (6) (2011) 46–51.

[7] M. Ovsik, M. Manas, M. Stanek, A. Dockal, J. Vanek, A. Mizera, M. Adamek, P. Stoklasek, Polyamide surface layer nano-indentation and thermal properties modified by irradiation, Materials 13 (13) (2020) 2915.

[8] C. Lu, T. Yang, K. Jin, N. Gao, P. Xiu, Y. Zhang, F. Gao, H. Bei, W.J. Weber, K. Sun, et al., Radiation-induced segregation on defect clusters in single-phase concentrated solid-solution alloys, Acta Mater. 127 (2017) 98–107.

[9] E. Aydogan, J.S. Weaver, U. Carvajal-Nunez, M.M. Schneider, J.G. Gigax, D.L. Krumwiede, P. Hosemann, T.A. Saleh, N.A. Mara, D.T. Hoelzer, B. Hilton, S. Maloy, Response of 14YWT alloys under neutron irradiation: A comple-

[10] H. Zhu, M. Qin, R. Aughterson, T. Wei, G. Lumpkin, Y. Ma, H. Li, Atomic origins of radiation-induced defects and the role of lamellar interfaces in radiation damage of titanium aluminide alloy irradiated with Kr-ions at elevated temperature, Acta Mater. 172 (2019) 72–83.

[11] P. Jung, J. Henry, J. Chen, Tensile properties of candidate structural materials for high power spallation sources at high helium contents, J. Nucl. Mater. 343 (1–3) (2005) 275–284.

[12] K.G. Field, X. Hu, K.C. Littrell, Y. Yamamoto, L.L. Snead, Radiation tolerance of neutron-irradiated model Fe–Cr–Al alloys, J. Nucl. Mater. 465 (2015) 746–755.

[13] T.D. De la Rubia, H.M. Zbib, T.A. Khraishi, B.D. Wirth, M. Victoria, M.J. Caturla, Multiscale modelling of plastic flow localization in irradiated materials, Nature 406 (6798) (2000) 871–874.

[14] D. Saad, H. Benkharfia, M. Izerrouken, A.A. Benyahia, H. Ait-Abderrahim, Displacement damage cross section and mechanical properties calculation of an Es-Salam research reactor aluminum vessel, Nucl. Sci. Tech. 28 (11) (2017) 1–9.

[15] K. Onizawa, H. Nishikawa, H. Itoh, Development of probabilistic fracture mechanics analysis codes for reactor pressure vessels and piping considering welding residual stress, Int. J. Pres. Ves. Pip. 87 (1) (2010) 2–10.

[16] J.R. Granada, Slow neutron total cross-section of Al6061 at low temperatures, J. Nucl. Mater. 277 (2–3) (2000) 346–350.

[17] P. Zhang, Y. Li, W. Wang, Z. Gao, B. Wang, The design, fabrication and properties of B4C/Al neutron absorbers, J. Nucl. Mater. 437 (1–3) (2013) 350–358.

[18] H.E. McCoy Jr, J.R. Weir Jr, Influence of irradiation on the tensile properties of the aluminum alloy 6061, Nucl. Sci. Eng. 25 (4) (1966) 319–327.

[19] C. Flament, J. Ribis, J. Garnier, Y. Serruys, F. Leprêtre, A. Gentils, C. Baumier, M. Descoins, D. Mangelinck, A. Lopez, et al., Stability of $\beta$ nano-phases in Al-Mg-Si (-Cu) alloy under high dose ion irradiation, Acta Mater. 128 (2017) 64–76.

[20] M.N. Gussev, N. Sridharan, S.S. Babu, K.A. Terrani, Influence of neutron irradiation on Al-6061 alloy produced via ultrasonic additive manufacturing, J. Nucl. Mater. 550 (2021) 152939.

[21] S.A. Briggs, P.D. Edmondson, K.C. Littrell, Y. Yamamoto, R.H. Howard, C.R. Daily, K.A. Terrani, K. Sridharan, K.G. Field, A combined APT and SANS investigation of $\alpha$ phase precipitation in neutron-irradiated model FeCrAl alloys, Acta Mater. 129 (2017) 217–228.

[22] Y. Cui, E. Aydogan, J.G. Gigax, Y. Wang, A. Misra, S.A. Maloy, N. Li, In situ micro-pillar compression to examine radiation-induced hardening mechanisms of FeCrAl alloys, Acta Mater. 202 (2021) 255–265.

[23] K. Yamakawa, I. Mukouda, Y. Shimomura, Void formation in neutron-irradiated Cu and Cu alloys, J. Nucl. Mater. 191 (1992) 396–400.

[24] W. Sun, Y. Zhu, R. Marceau, L. Wang, Q. Zhang, X. Gao, C. Hutchinson, Precipitation strengthening of aluminum alloys by room-temperature cyclic plasticity, Science 363 (6430) (2019) 972–975.

[25] Y. Isobe, M. Sagisaka, F.A. Garner, S. Fujita, T. Okita, Precipitate evolution in low-nickel austenitic stainless steels during neutron irradiation at very low dose rates, J. Nucl. Mater. 386 (2009) 661–665.

[26] V.M. Lebedev, V.T. Lebedev, I.N. Ivanova, S.P. Orlov, D.N. Orlova, Structure of aluminum alloys irradiated with reactor neutrons, Phys. Solid State 52 (5) (2010) 996–999.

[27] K.V. Tsay, O.V. Rofman, V.V. Kudryashov, A.V. Yarovchuk, O.P. Maksimkin, Influence of neutron irradiation and ageing on behavior of SAV-1 reactor alloy, Nucl. Eng. Technol. (2021) inpress.

[28] J. Thomas, A.F. Bengoa, S.T. Nori, R. Ren, P. Kenesei, J. Almer, J. Hunter, J. Harp, M.A. Okuniewski, The application of synchrotron micro-computed tomography to characterize the three-dimensional microstructure in irradiated nuclear fuel, J. Nucl. Mater. 537 (2020) 152161.

[29] S. Johns, L. He, K. Bustillo, W.E. Windes, R. Ubic, C. Karthik, Fullerene-like defects in high-temperature neutron-irradiated nuclear graphite, Carbon 166 (2020) 113–122.

[30] J.D. Arregui-Mena, D.A. Cullen, R.N. Worth, S.V. Venkatakrishnan, M.S. Jordan, M. Ward, C.M. Parish, N. Gallego, Y. Katoh, P.D. Edmondson, et al., Electron tomography of unirradiated and irradiated nuclear graphite, J. Nucl. Mater. 545 (2021) 152649.

[31] P.D. Edmondson, A. London, A. Xu, D.E.J. Armstrong, S.G. Roberts, Small-scale characterisation of irradiated nuclear materials: Part I–microstructure, J. Nucl. Mater. 462 (2015) 369–373.

[32] J. Wade-Zhu, R. Krishna, A.J. Bodey, M. Davies, N.K. Bourne, C. Rau, B. Davies, A. Tzelepi, A.N. Jones, B.J. Marsden, et al., 4D synchrotron X-ray microtomography of fracture in nuclear graphite after neutron irradiation and radiolytic oxidation, Carbon 168 (2020) 230–244.

[33] A.K. Agrawal, B. Singh, Y.S. Kashyap, M. Shukla, B.S. Manjunath, S.C. Gadkari, Gamma-irradiation-induced micro-structural variations in flame-retardant polyurethane foam using synchrotron X-ray micro-tomography, J. Synchrotron Radiat. 26 (5) (2019) 1797–1807.

[34] H.W. Chai, Z.L. Xie, X.H. Xiao, H.L. Xie, J.Y. Huang, S.N. Luo, Microstructural characterization and constitutive modelling of deformation of closed-cell foams based on in situ x-ray tomography, Int. J. Plast. (2020) 102730.

[35] R.C. Chen, L. Rigon, R. Longo, Quantitative 3D refractive index decrement reconstruction using single-distance phase-contrast tomography data, J. Phys. D Appl. Phys. 44 (49) (2011) 495401.

[36] J.C. Cheng, H.W. Chai, G.L. Fan, Z.Q. Li, H.L. Xie, Z.Q. Tan, B.X. Bie, J.Y. Huang, S.N. Luo, Anisotropic spall behavior of CNT/2024Al composites under plate impact, Carbon 170 (2020) 589–599.

[37] B.X. Bie, J.Y. Huang, D. Fan, T. Sun, K. Fezzaa, X.H. Xiao, M.L. Qi, S.N. Luo, Orientation-dependent tensile deformation and damage of a T700 carbon fiber/epoxy composite: A synchrotron-based study, Carbon 121 (2017) 127–133.

[38] R.C. Chen, D. Dreossi, L. Mancini, R. Menk, L. Rigon, T.Q. Xiao, R. Longo, PITRE: Software for phase-sensitive X-ray image processing and tomography reconstruction, J. Synchrotron Radiat. 19 (5) (2012) 836–845.

[39] A. Buades, B. Coll, J.-M. Morel, A non-local algorithm for image denoising, in: 2005 IEEE Computer Society Conference on Computer Vision and Pattern Recognition (CVPR'05), vol. 2, IEEE, 2005, pp. 60–65.

[40] D.S. Bright, E.B. Steel, Two-dimensional top hat filter for extracting spots and spheres from digital images, J. Microsc. 146 (2) (1987) 191–200.

[41] J. Vymeětal, J. Vondraášek, Gyration-and inertia-tensor-based collective coordinates for metadynamics. application on the conformational behavior of polyalanine peptides and Trp-cage folding, J. Phys. Chem. A 115 (41) (2011) 11455–11465.

[42] H.Y. Li, H.W. Chai, X.H. Xiao, J.Y. Huang, S.N. Luo, Fractal breakage of porous carbonate sand particles: microstructures and mechanisms, Powder Technol. 363 (2020) 112–121.

[43] Y. Osada, EPMA mapping of small particles of $\alpha$-AlFeSi and $\beta$-AlFeSi in AA6063 alloy billets, J. Mater. Sci. 38 (7) (2003) 1457–1464.

[44] Y. Wang, M.J. Emerson, K. Conradsen, A.B. Dahl, V.A. Dahl, E. Maire, P.J. Withers, Evolution of fibre deflection leading to kink-band formation in unidirectional glass fibre/epoxy composite under axial compression, Compos. Sci. Technol. 213 (2021) 108929.

[45] Y.W. Yan, L. Geng, A.B. Li, Experimental and numerical studies of the effect of particle size on the deformation behavior of the metal matrix composites, Mater. Sci. Eng. A 448 (1–2) (2007) 315–325.

[46] N. Chawla, K.K. Chawla, Microstructure-based modeling of the deformation behavior of particle reinforced metal matrix composites, J. Mater. Sci. 41 (3) (2006) 913–925.

[47] R. Hedayati, S.A. Yavari, A.A. Zadpoor, Fatigue crack propagation in additively manufactured porous biomaterials, Mater. Sci. Eng. C 76 (2017) 457–463.

[48] J.H. Zhao, Z.L. Xie, T. Zhong, T. Sun, K. Fezzaa, Y. Cai, J.Y. Huang, S.N. Luo, Strain rate effects on the mechanical behavior of porous titanium with different pore sizes, Mater. Sci. Eng. A 821 (2021) 141593.

[49] S.W. Park, L. Linsen, O. Kreylos, J.D. Owens, B. Hamann, Discrete sibson interpolation, IEEE T. Vis. Comput. Gr. 12 (2) (2006) 243–253.

[50] F.F.J. Schrijer, F. Scarano, Effect of predictor–corrector filtering on the stability and spatial resolution of iterative PIV interrogation, Exp. Fluids 45 (5) (2008) 927–941.

[51] N.P. van Dijk, D. Wu, C. Persson, P. Isaksson, A global digital volume correlation algorithm based on higher-order finite elements: implementation and evaluation, Int. J. Solids Struct. 168 (2019) 211–227.